OPEN ACCESS

University of BRISTOL

Peer reviewed version

Link to published version (if available):
10.1073/pnas.1916711117

Link to publication record in Explore Bristol Research
PDF-document

University of Bristol - Explore Bristol Research
General rights

Main Manuscript for

First direct kinetic measurements and theoretical predictions of an isoprene-derived Criegee intermediate

Rebecca L. Caravan[a,b,c], Michael F. Vansco[d], Kendrew Au[b], M. Anwar H. Khan[e], Yu-Lin Li[f,g], Frank A. F. Winiberg[h,i], Kristen Zuraski[a], Yen-Hsiu Lin[f,g], Wen Chao[f], Nisalak Trongsiriwat[d], Patrick J. Walsh[d], David L. Osborn[b], Carl J. Percival[h], Jim Jr-Min Lin[f,g], Dudley E. Shallcross[e], Leonid Sheps[b], Stephen J. Klippenstein[c], Craig A. Taatjes[b] & Marsha I. Lester[d*].

[a]NASA Postdoctoral Program Fellow, NASA Jet Propulsion Laboratory, California Institute of Technology, 4800 Oak Grove Drive, Pasadena, CA 91109, USA.
[b]Combustion Research Facility, Mailstop 9055, Sandia National Laboratories, Livermore, CA 94551, USA.
[c]Chemical Sciences and Engineering Division, Argonne National Laboratory, Lemont, IL 60439, USA.
[d]Department of Chemistry, University of Pennsylvania, Philadelphia, PA 19104-6323, USA.
[e]School of Chemistry, Cantock's Close, University of Bristol, Bristol BS8 1TS, UK.
[f]Institute of Atomic and Molecular Sciences, Academia Sinica, Taipei 10617, Taiwan.
[g]Department of Chemistry, National Taiwan University, Taipei 10617, Taiwan.
[h]NASA Jet Propulsion Laboratory, California Institute of Technology, 4800 Oak Grove Drive, Pasadena, CA 91109, USA.
[i]California Institute of Technology, Pasadena, CA 91125.

* Correspondence to Marsha I. Lester
Email: milester@sas.upenn.edu

Rebecca L. Caravan: https://orcid.org/0000-0002-2936-7952
Michael F. Vansco: https://orcid.org/0000-0002-6189-6272
M. Anwar H. Khan: https://orcid.org/0000-0001-7836-3344
Frank A. F. Winiberg: https://orcid.org/0000-0003-2801-5581
Patrick J. Walsh: https://orcid.org/0000-0001-8392-4150
David L. Osborn: https://orcid.org/0000-0003-4304-8218
Carl J. Percival: https://orcid.org/0000-0003-2525-160X
Jim Jr-Min Lin: https://orcid.org/0000-0002-8308-2552
Dudley E. Shallcross: https://orcid.org/0000-0001-7614-9221
Leonid Sheps: https://orcid.org/0000-0003-4320-0865
Stephen J. Klippenstein: https://orcid.org/0000-0001-6297-9187
Craig A. Taatjes: https://orcid.org/0000-0002-9271-0282
Marsha I. Lester: https://orcid.org/0000-0003-2367-3497

Classification
PHYSICAL SCIENCES; Chemistry.

Author Contributions
Rebecca L. Caravan: Designed and performed experiments, analyzed the data and wrote the paper.
Michael F. Vansco: Designed and performed experiments, analyzed the data and wrote the paper.
Kendrew Au: Performed experiments.
M. Anwar H. Khan: Performed global chemistry and transport work and wrote the paper.
Yu-Lin Li: Performed experiments and analyzed the data.
Frank A. F. Winiberg: Performed experiments.
Kristen Zuraski: Performed experiments.
Yen-Hsiu Lin: Performed experiments and analyzed the data.
Wen Chao: Designed experiments.
Nisalak Trongsiriwat: Designed the synthesis of and contribute the MVK-oxide precursor.
Patrick J. Walsh: : Designed the synthesis of and contribute the MVK-oxide precursor.
David L. Osborn: Designed and performed experiments.
Carl J. Percival: Designed and performed experiments.
Jim Jr-Min Lin: Designed experiments and wrote the paper.
Dudley E. Shallcross: Performed global chemistry and transport work.
Leonid Sheps: Performed experiments and analyzed the data.
Stephen J. Klippenstein: Performed *ab initio* kinetics calculations and wrote the paper.
Craig A. Taatjes: Designed and performed experiments, analyzed the data and wrote the paper.
Marsha I. Lester: Designed and performed experiments, analyzed the data and wrote the paper.

This PDF file includes:
 Main Text
 Figures 1 to 8
 Schemes 1 to 5

Abstract

Isoprene has the highest emission into Earth's atmosphere of any non-methane hydrocarbon. Atmospheric processing of alkenes, including isoprene, via ozonolysis leads to the formation of zwitterionic reactive intermediates, known as Criegee intermediates (CIs). Direct studies have revealed that reactions involving simple CIs can significantly impact the tropospheric oxidizing capacity, enhance particulate formation and degrade local air quality. Methyl vinyl ketone oxide (MVK-oxide) is a four-carbon, asymmetric, resonance-stabilized CI, produced with 21-23% yield from isoprene ozonolysis, yet its reactivity has not been directly studied. We present direct kinetic measurements of MVK-oxide reactions with key atmospheric species using absorption spectroscopy. Direct UV-Vis absorption spectra from two independent flow-cell experiments overlap with the molecular-beam UV-Vis-depletion spectra reported recently (Vansco MF, Marchetti B, & Lester MI (2018) Electronic spectroscopy of methyl vinyl ketone oxide: a four-carbon unsaturated Criegee intermediate from isoprene ozonolysis. *The Journal of Chemical Physics* 149(24):244309), but suggest different conformer distributions under jet-cooled and thermal conditions. Comparison of the experimental lifetime herein with theory indicates only the *syn*-conformers are observed; *anti*-conformers are calculated to be removed much more rapidly via unimolecular decay. We observe experimentally and predict theoretically fast reaction of *syn*-MVK-oxide with SO_2 and formic acid, similar to smaller alkyl-substituted CIs, and by contrast, slow removal in the presence of water. We determine products through complementary multiplexed photoionization mass spectrometry; observing SO_3 and identifying organic hydroperoxide formation from reaction with SO_2 and formic acid, respectively. The tropospheric implications of these reactions are evaluated using a global chemistry and transport model.

Significance statement

Ozonolysis is an important sink of alkenes in Earth's troposphere, leading to the formation of Criegee intermediates (CIs), whose reactions significantly impact tropospheric composition. The reactivity of the four-carbon unsaturated CIs derived from isoprene, the most abundant alkene, has remained unknown until now. The first direct measurements of one such CI, methyl vinyl ketone oxide (MVK-oxide), with water vapor, SO_2, and formic acid are reported herein, substantiated by high-level theory, revealing the long lifetime of *syn*-MVK-oxide with respect to unimolecular decay and reaction with water vapor. Through a combination of direct experiment, high-level theory and global modelling, *syn*-MVK-oxide is shown to survive high-humidity tropospheric environments and play a role in sulfuric acid formation and formic acid removal.

Introduction/background

Isoprene is a five carbon, doubly unsaturated hydrocarbon with the highest emission into Earth's atmosphere of any non-methane hydrocarbon. Its sources are predominantly biogenic, totaling 530 Tg per year (1), with abundances peaking between the tropics over the landmass where most of the Earth's biomass is located (e.g., the Amazon). An important sink of tropospheric isoprene (~10% (2)) is reaction with ozone, proceeding via 1,3-cycloaddition of ozone to either of the two C=C double bonds to give a primary ozonide (POZ). The POZ subsequently decomposes to form a carbonyl species and a carbonyl oxide – a zwitterionic reactive intermediate, known as a Criegee intermediate (CI) (3). Depending on the double bond to which ozone adds, and how the POZ decomposes, four pairs of reaction products are possible: formaldehyde oxide (CH_2OO) + methyl vinyl ketone, formaldehyde oxide + methacrolein, methacrolein oxide ($HC(OO)C(CH_2)CH_3$) + formaldehyde, or methyl vinyl ketone oxide (MVK-oxide, $CH_3C(OO)CHCH_2$) + formaldehyde (Scheme 1). The resulting chemically activated Criegee intermediate can undergo either rapid unimolecular decomposition or can be thermalized through collisions to form so-called stabilized Criegee intermediates, that can subsequently undergo unimolecular and bimolecular reactins. Here, we report the first direct measurements of unimolecular and bimolecular reactions of stabilized MVK-oxide at 298 K.

Global and local CI concentrations have previously been estimated via chemistry and transport models, using databases of alkene emissions (4). Concentration maxima are predicted in forested regions such as the Amazon, correlating with high isoprene emissions. With steady state CI concentrations $\leq 10^4$ cm^{-3} (4-8), two orders of magnitude lower than that of the principal tropospheric oxidant OH, reactivity of CIs with key pollutants needs to be substantial to impact tropospheric lifetimes in comparison to OH-initiated processing. Low steady-state concentrations of CIs, resulting from slow production via ozonolysis and rapid subsequent decomposition, had until recently inhibited study of CI reactivity. Direct methods to

3

photolytically generate simple CIs with carbon backbones containing up to three carbons (9-12) have enabled studies that revealed CI reactivity to be far greater than previously thought. Consequently the flux of pollutant species, such as SO_2, through reaction with Criegee intermediates could be significant.

The reaction of CH_2OO with the critical tropospheric pollutant SO_2 was shown to be 10,000 times faster than inferred from ozonolysis studies (11) and leads to the formation of SO_3 – a critical sulfuric acid precursor in the troposphere that results in sulfate aerosol production (13-16). Subsequent chemistry and transport modelling suggests that tropospheric processing of SO_2 to SO_3 by CIs is comparable to SO_2 removal by OH in areas where CI concentrations are largest (4). CI + SO_2 reactions can account for as much as 46% of sulfuric acid production at ground level (15) – increasing modelled particle nucleation rates by up to 820% (17) and thus, impacting air quality, climate and human health.

Reactions of CIs with organic acids have also been implicated in the formation of aerosols (18, 19). Fast removal of CIs by reaction with a number of organic acids has been measured (18-20). Global chemistry and transport modelling reveals that these reactions could significantly reduce modelled organic acid concentrations (18), with the greatest impacts over the Amazon area where CI concentrations are the highest (18). Through a combination of experimental and theoretical work for reactions of simple 1-3 carbon CIs, a mechanism has been identified whereby the CI inserts into the acidic O-H bond (18-20), leading to highly oxygenated, lower volatility, functionalized organic hydroperoxides.

Due to the relatively high abundance of water in the troposphere, CI removal by reactions with water monomer and dimer can dominate over other reactive loss processes even for modest rate coefficients, constraining CI availability for other bimolecular reactions. However, through experimental work and theoretical studies, the rate coefficients for reaction of CIs with both water monomer and dimer have been shown to vary by orders of magnitude, depending on substituents and conformer of the CI. For example, a combination of experimental and theoretical studies of the two-carbon CI, acetaldehyde oxide, has shown that reactivity of the *syn-* and *anti-*conformers with water could differ by as much as five orders of magnitude (4, 10, 21-28). Therefore, the potential tropospheric impact of CIs is highly dependent on their structures.

MVK-oxide, a resonance-stabilized, four-carbon CI, is estimated to be produced from 21-23% of isoprene ozonolysis reactions under tropospheric conditions (2, 29). At present, local and global chemical models of the atmosphere represent the reactivity of four-carbon and higher, functionalized CIs based on direct measurements of the smaller H- or alkyl-substituted CIs. In MVK-oxide, the Criegee intermediate COO functional group is resonance stabilized with the vinyl side chain, potentially influencing reactivity, and thus, its role as a tropospheric oxidant. No direct measurements (22) have been performed on the reactions of resonance stabilized CIs.

Like acetaldehyde oxide, MVK-oxide exists as distinct *syn-* and *anti-*conformers that do not interconvert at 298 K; *syn* and *anti* refer to the orientation of the terminal CI oxygen with respect to the methyl group of the carbon backbone. Each MVK-oxide conformer comprises two further configurations for the orientation of the vinyl group, *cis* and *trans*, that rapidly interconvert by rotation about the C-C bond at ~ 298 K ((6), see SI Appendix). Until recently, no synthetic methods for the isolated production of MVK-oxide were known – preventing the direct study of the reactivity of either conformer. Barber *et al.* (30) recently reported a scheme for the selective production of MVK-oxide and employed this method to record an IR-action spectrum. The same scheme was used by Vansco *et al.* (31) to obtain a UV-Vis depletion spectrum, which displayed broad absorption features from 300-450 nm, consistent with both *syn-* and *anti-*conformers. Both studies generated MVK-oxide via 248 nm photolysis of 1,3 diiodobut-2-ene in O_2/Ar carrier gas that was sampled following supersonic expansion (T~ 10 K) under collision free conditions. Vansco *et al.* (31) recorded the UV-Vis induced depletion of the MVK-oxide photoionization signal (at 10.5 eV) on the m/z 86 (parent ion of MVK-oxide) mass channel. Additional studies indicated that MVK-oxide rapidly dissociates upon UV-Vis excitation to $O(^1D)$ products, providing evidence that the depletion measurements can be directly related to absorption.

For MVK-oxide, theory predicts relatively slow loss of both *syn-* and *anti-*conformers by reactions with water monomer and dimers – leading to first order loss rates of ≤ 1 s^{-1} in the troposphere (6, 32). However, rapid unimolecular decay represents a potentially significant competitive loss process: thermal unimolecular loss rates at 298 K of 33 s^{-1} and 2140 s^{-1} for *syn-* and *anti-*MVK-oxide conformers, respectively, have been calculated (30). Experimental observations to substantiate these unimolecular and water reaction loss rates, and to determine bimolecular reaction rate coefficients with key pollutant species, are therefore needed to evaluate the role of MVK-oxide in the troposphere.

The present study builds on the work of Vansco *et al.* (31) and reports direct absorption spectra of MVK-oxide at 298 K, obtained using two separate experiments (33-35). Using the characterized direct UV-Vis absorption spectra, we have employed broadband absorption spectroscopy to conduct direct bimolecular kinetics studies of MVK-oxide with key tropospheric species: SO_2, formic acid and water. Complementary experiments using multiplexed photoionization mass spectrometry (MPIMS) and *ab initio* kinetic studies have been conducted to identify products resulting from reaction with SO_2 and formic acid and infer mechanisms. The implications of MVK-oxide reactivity on global sulfate aerosol formation and formic acid removal have been evaluated by a global 3-dimensional chemistry and transport model, STOCHEM-CRI.

Results/discussion

Spectroscopy and unimolecular decay
MVK-oxide spectroscopy. The MVK-oxide electronic spectra recorded by direct absorption at 298 K using both the Sandia (34) and IAMS (35) experimental apparatus span the same spectral range (300-450 nm) as that reported recently by Vansco *et al.* (31) using a depletion method under jet-cooled conditions (Figure 1). The 298 K spectrum has a broad symmetric absorption from 300-450 nm, peaking at 370 nm with FWHM of 80 nm. The electronic spectrum obtained by Vansco *et al.* (31) has a similarly broad, but asymmetric profile peaked at 388 nm. We anticipate that the MVK-oxide conformer distribution may differ significantly at 298 K and under jet-cooled experimental conditions. We propose that this difference originates from the fast unimolecular decay of *anti*-conformers compared to *syn*-conformers at 298 K, discussed herein, and the rapid interconversion of *cis* and *trans* configurations.

The unimolecular decay mechanisms, transition state (TS) barriers, and thermal unimolecular decay rate coefficients for the *syn*- and *anti*-conformers of MVK-oxide differ considerably from one another. For *syn*-MVK-oxide conformers, unimolecular decay follows a 1,4 H-atom transfer mechanism that eventually releases OH radicals (Scheme 2). Thus, bimolecular reactions that compete with unimolecular decay in the troposphere will intercept OH production, and may impact the oxidizing capacity of the troposphere. The thermal decay rate for *syn*-MVK-oxide was experimentally benchmarked by the rate of appearance of OH products upon IR-activation of *syn*-MVK-oxide, which agreed with an RRKM calculation based on an *ab initio* predicted TS barrier of 18.0 kcal mol^{-1} (30). Master equation calculations predicted a thermal unimolecular decay rate for *syn*-MVK-oxide of 33 s^{-1} (298 K, 1 atm, with ~10% reduction at 10 torr), which includes substantial contribution from H-atom tunneling. By contrast, theory predicts that *anti*-MVK-oxide conformers decay via a 1,5 electrocyclic ring closure process that forms a cyclic peroxide (Scheme 3), known as dioxole (6, 30, 36), with a TS barrier of only 12.0 kcal mol^{-1} and thermal decay rate of 2140 s^{-1} (298 K, 1 atm) (30).

The transient absorption time trace for MVK-oxide obtained at 298 K in the Sandia experiment reveals a slow decay on the millisecond timescale as shown in Figure 1 (lower panel, inset, and reproduced larger in the SI Appendix). The experimental time profile agrees with a simulation using the predicted rate coefficient for *syn*-MVK-oxide of 33 s^{-1} (298 K), shown as a cyan line in the inset of Figure 1 (30, 36). Based on the theoretically predicted thermal decay rate coefficient for *anti*-MVK-oxide of 2140 s^{-1} (298 K) (30), the time-resolved experiments should also exhibit a fast decay component, which is not observed. This suggests a faster decay rate possibly due to initial internal excitation of *anti*-MVK-oxide and/or low yield of the stabilized *anti*-conformer in the present 298 K experiments. This differs from prior studies under jet-cooled conditions with short delay-times (20 μs) between generation and probing , where spectroscopic features attributed to both *syn*- and *anti*-conformers of MVK-oxide were observed (30, 31). Comparison of the direct absorption and depletion measurements of the MVK-oxide electronic spectrum indicates that they match in the shorter wavelength region, suggesting that *syn*-conformers likely dominate at λ < 375 nm in both experiments. At λ > 375 nm, a combination of *syn*- and *anti*-conformers appear to contribute to the jet cooled spectrum, while predominantly *syn*-conformers give rise to the spectrum at 298 K. Theoretical calculations predict vertical transitions for the more stable *syn-trans*-conformer at shorter wavelengths (350 nm) and *anti-trans*-conformer at longer wavelengths (381 nm), although the computed electronic spectra (31) suggest they will be broad and overlapping. Rapid removal of *anti*-conformers at 298 K is consistent with the observed spectral changes, and suggests that bimolecular reactions with the *anti*-conformer are unlikely to compete with unimolecular decay in the troposphere.

SO$_2$ scavenger experiments. Previous measurements of simple CIs have demonstrated rapid reaction with SO_2 (10, 11, 37, 38). To substantiate the assignment of the broad spectral feature to MVK-oxide, SO_2

was added to act as a scavenger for MVK-oxide in the IAMS experiments. Sufficient SO_2 was added to reduce the lifetime of MVK-oxide to <0.03 ms, assuming that the rate coefficient for MVK-oxide + SO_2 was comparable to that for CH_2OO + SO_2 (11, 38). Time-resolved spectra in the absence of SO_2 (Figure 2, upper panel), show the broad absorption feature assigned to MVK-oxide at 370 nm and its decay due to various experimental loss processes (i.e., wall loss and reactions with I atoms). The transient absorption spectra also show depletion signals at λ<320 nm due to the precursor, structured features due to IO (λ ~410-450 nm) (39) and a broad feature from I_2 side-product (λ ~450-600 nm) (40). Note that even in the absence of SO_2, the decay in the IAMS experiment is more rapid than that observed in the Sandia absorption experiment (Figure 1, lower panel, inset and SI Appendix). In the latter, the experimental conditions were optimized to minimize bimolecular loss channels in order to observe unimolecular decay. In the presence of SO_2 (Figure 2, lower panel), the broad spectral feature centered at λ ~370 nm is absent – providing further evidence that this feature is due to MVK-oxide. Furthermore, the complete removal of this feature in <0.5 ms indicates that the bimolecular rate coefficient for MVK-oxide + SO_2 is rapid, as detailed below. By subtraction of the spectra in Figure 2 (lower panel from those in the upper panel), the features due to MVK-oxide are obtained, as shown in Figure 1. Note, this subtraction process does not perfectly remove spectral components due to IO, and so residual signal due to IO absorption at longer wavelengths has been manually removed to obtain the IAMS data presented in Figure 1.

Bimolecular Kinetics

Using the direct UV-Vis absorption spectrum of *syn*-MVK-oxide, bimolecular kinetics with SO_2 and formic acid were investigated via broadband absorption spectroscopy. These experiments reveal that *syn*-MVK-oxide reactivity towards these species is similar to that of the smaller, H/alkyl-substituted CIs. Preliminary experiments also provide an upper limit for the very slow reaction of *syn*-MVK-oxide with water. The experimental observations are supported by high-level *ab initio* calculations that reveal much slower removal with water than for smaller CIs. Complementary investigations using MPIMS were undertaken to probe the products of the *syn*-MVK-oxide + SO_2 and formic acid reactions and further mechanistic insight is provided through high level *ab initio* kinetics calculations. Additional MPIMS experiments were performed to obtain the formation kinetics of MVK-oxide from the reaction of the iodoalkenyl radical with O_2, the results of which are discussed in the supporting information (SI Appendix).

MVK-oxide + SO_2. Rapid removal of *syn*-MVK-oxide in the presence of SO_2 was observed from both the Sandia (10 Torr He/O_2) and IAMS (7 Torr N_2/O_2) experiments (Figure 3). The pressure-dependence of the *syn*-MVK-oxide + SO_2 rate coefficient across the total pressure range 4-700 Torr N_2 was investigated using the IAMS direct absorption experiment and no significant dependence on pressure was observed. A rate coefficient of $(4.2 \pm 0.6) \times 10^{-11}$ cm^3s^{-1} (95% confidence limit error bar) at 298 K across the total pressure range 300-700 Torr N_2 is derived. This rate coefficient is supported by high-level computational kinetics calculations, is comparable with that reported for smaller CIs (4, 10, 11, 27, 33, 37, 38, 41, 42), and is consistent with barrierless addition of MVK-oxide to SO_2, initially forming a secondary ozonide (SOZ) structure (Figure 4 and Scheme 4). *Ab initio* calculations along the reaction coordinate reveal that the transition state (TS) barrier(s) are comparatively higher for MVK-oxide + SO_2 vs. CH_2OO + SO_2 due to disruption of the extended conjugation of MVK-oxide. However, because the CH_2OO and MVK-oxide (Figure 4) reactions proceed through strongly submerged barriers relative to the reactants, this results in minimal perturbation of the overall bimolecular rate coefficients.

Interrogation of the reaction products was undertaken through complementary MPIMS experiments at 10 Torr: SO_3 production was observed, with rise times consistent with CI loss kinetics, confirming SO_3 as a direct reaction product from *syn*-MVK-oxide + SO_2 (Figure 3). Through rapid reaction of SO_3 with water in the troposphere, this reaction could represent a significant source of atmospheric sulfuric acid. Under the low-pressure conditions of these experiments, there was no substantive evidence for stabilized SOZ. To explore the pressure-dependent branching between SOZ stabilization and SO_3 + MVK formation, we implemented an *ab initio* transition state theory-based master equation (AITSTME) model for the overall kinetic process. At 10 Torr, the AITSTME model demonstrates minimal stabilization of the SOZ (see SI Appendix), supporting the experimental observations. Under tropospheric conditions, the higher density of states in the SOZ formed from larger CI reactions with SO_2 is predicted to result in increased SOZ lifetime (32), and third body collisions are expected to form stabilized SOZ. At 300 K and 1 atm, *ab initio* kinetics calculations predict a ~5 % yield of SOZ. However, the tropospheric fate of the SOZ remains uncertain with respect to decomposition or further reaction. The total rate coefficient is predicted to be effectively pressure-independent, with no back reaction from the SOZ to the reactants. However, there is predicted

to be a fairly strong temperature-dependence due to the effect of TS1 connecting the pre-reactive complexes and SOZ (see SI Appendix).

MVK-oxide + formic acid. The kinetics of *syn*-MVK-oxide + formic acid were measured using the Sandia absorption experiment, yielding a rate coefficient of $(3.0 \pm 0.1) \times 10^{-10}$ cm^3 s^{-1} (Figure 5). Reaction near the gas kinetic limit is consistent with the rapid reaction of smaller CIs with organic acids reported previously (18, 19). High level *ab initio* calculations confirm the barrierless insertion of the CI into the O-H bond of formic acid (Figure 6 and Scheme 5), leading to a functionalized hydroperoxide, hydroperoxybut-3-en-2-yl formate (HPBF). However the resonance-stabilization in MVK-oxide significantly alters the potential energy surface of this reaction, compared to the CH$_2$OO case (43). For the CH$_2$OO reaction, Vereecken *et al.*(6) found that the primary reaction pathway involves H-transfer from the acid to the CI in concert with CO bond formation, followed by stabilization of the resulting functionalized hydroperoxide species. The functionalized hydroperoxide is much more weakly bound in the MVK-oxide reaction than in its CH$_2$OO analogue (30 versus 44 kcal mol^{-1} (43)), due to the additional resonance stabilization present in MVK-oxide. In the CH$_2$OO case, stabilization of the adduct is predicted to dominate over bimolecular product formation, even though there is an exothermic exit channel arising from OO bond fission of the functionalized hydroperoxide. In the MVK-oxide case, the functionalized hydroperoxide is also favored over dissociation to produce OH + an alkoxy radical, which is now significantly endothermic relative to reactants. Despite these differences, the overall kinetics are predicted to be quite similar, with the reaction dominated by direct addition to form the functionalized hydroperoxide, HPBF in the case of MVK-oxide (discussed in further detail in the SI Appendix).

This reaction mechanism is supported by complementary MPIMS experiments that reveal the formation of species at exact masses corresponds to C$_4$H$_7$O$_2$ and C$_5$H$_7$O$_2$ (Figure 5, top right inset). These products are consistent with characteristic HCO$_2$-loss (= protonated CI) and HO$_2$-loss daughter ions (DIs) from the dissociative photoionization of the predicted functionalized hydroperoxide reaction product, HPBF (18, 19, 44). The formation of the hydroperoxide product is further evidenced by the agreement between the observed and calculated vertical ionization energies and appearance energies for the m/z 99 daughter ion (further details in SI Appendix).

Master equation-based predictions for the temperature- and pressure-dependencies of the *syn*-MVK-oxide + formic acid recombination rate coefficient are illustrated in Figure 7. Notably, near room temperatures, at pressures near 10 Torr (0.013 bar), the predicted rate coefficient is essentially identical to the experimentally observed value and strongly pressure-dependent. Although the present calculations were performed for N$_2$ as a collider, the variation between N$_2$ and He, should be quite modest. Importantly, at atmospheric pressure, the pressure-dependence is greatly reduced with the rate coefficient effectively determined by the capture rate. At 1 bar, the predicted temperature-dependence is well represented by the expression 7.7×10^6 T$^{-5.86}$ exp(-1170/T) cm^3 s^{-1} over the 200 to 400 K temperature region, with a predicted value of 4.9×10^{-10} cm^3 s^{-1} at room temperature.

MVK-oxide + water. Slow removal of *syn*-MVK-oxide in the presence of water vapor (where [H$_2$O] ≤ 5.7 $\times$ 10^{17} cm^{-3}, [(H$_2$O)$_2$] ≤ 7.9$\times$10^{14} cm^{-3}) was observed experimentally and upper limits of 4.0×10^{-17} cm^3 s^{-1} and 3.0×10^{-14} cm^3 s^{-1} are derived from IAMS absorption experiments. These results are consistent with previous theoretical predictions of 9.5×10^{-20} cm^3 s^{-1} and 9.0×10^{-17} cm^3 s^{-1} for the water monomer and dimer reaction rate coefficients (6, 45), respectively (or 8.1×10^{-20} cm^3 s^{-1} and 3.1×10^{-16} cm^3 s^{-1}, respectively, following adjustments made by Vereecken *et al.* to account for the level of theory used, see SI Appendix). Higher level kinetics calculations performed herein (see SI Appendix for further details) return a rate coefficient of 1.1×10^{-19} cm^3 s^{-1} for the *syn*-MVK-oxide + water monomer reaction, supporting the literature theoretical values (6, 45) and experimental upper limits reported here. By contrast, CH$_2$OO reacts rapidly with water and water dimer, with bimolecular rate coefficients of 2.4×10^{-16} and 6.6×10^{-12} cm^3 s^{-1}, respectively, reported in the literature (46, 47), and thus these reactions are a significant atmospheric sink of CH$_2$OO. We attribute the smaller reactivity of MVK-oxide vs. CH$_2$OO with water vapor to a higher transition state (TS) barrier arising from disruption of the extended conjugation of *syn*-MVK-oxide in reaction leading to the hydroperoxide adduct. A pre-reactive complex exists for both reactions and both have similar stabilities (-6.52 kcal mol^{-1} for CH$_2$OO vs. -6.11 kcal mol^{-1} for MVK-oxide). At the TS, the carbonyl oxide moiety begins bending out of plane, indicating that the extended conjugation is disrupted in the case of MVK-oxide. As a result, the TS barrier for the MVK-oxide + H$_2$O reaction is significantly higher (10.53 kcal mol^{-1} for MVK-oxide vs. 3.12 kcal mol^{-1} for CH$_2$OO), which dramatically lowers the reaction rate compared to CH$_2$OO + H$_2$O. Reaction with water will therefore not be an

important sink of *syn*-MVK-oxide in the troposphere, and thus, MVK-oxide will survive high-humidity environments; this implies a relatively high tropospheric concentration of *syn*-MVK-oxide.

Atmospheric modelling

The role of MVK-oxide in the troposphere has been evaluated through comparison of two model integrations, detailed herein. STOCHEM-CI0 represents our best current understanding of CI chemistry. It includes the reactions of MVK-oxide with SO_2, formic acid, water and water dimer, in addition to unimolecular loss. STOCHEM-CI1 is a base-case scenario model wherein the reactions of MVK-oxide with SO_2 and formic acid are omitted (but still includes unimolecular decay and reactions with water and water dimer). In the model, *syn*- and *anti*-MVK-oxide are assumed to be produced from isoprene ozonolysis with yields of 0.14 and 0.07, respectively (29). The kinetic parameters utilized in both model integrations are detailed in the SI Appendix.

Evaluation of STOCHEM-CI0 reveals that, globally, MVK-oxide has the largest modelled steady-state concentration of all stabilized CIs (33% of the total CI molecules, 49% by weight). This is due to large isoprene emissions over forested regions, and slow tropospheric removal through unimolecular decomposition and reactions with water and water dimer. If removal with SO_2 and formic acid are neglected (STOCHEM-CI1), the steady-state concentration of MVK-oxide increases slightly (36% of total CI molecules, 54% by weight). The slow removal via bimolecular reactions with water and water dimer, and via unimolecular decomposition (33 s^{-1} at 298 K for *syn*-MVK-oxide (30) vs. ca. 300 s^{-1} for acetone oxide (37, 48, 49)) means that MVK-oxide will survive in high humidity environments and thus other bimolecular reactions may be important.

We find that MVK-oxide plays a role in the tropospheric conversion of SO_2 to sulfuric acid (Figure 8, upper panel), the removal of formic acid (Figure 8, lower panel) and potentially, particulate formation. Evaluation of STOCHEM-CI0 reveals that the reaction with SO_2 increases the SO_3 formation flux by 93% compared with the base-case scenario (STOCHEM-CI1), despite reaction with SO_2 accounting for only ~2% of the total tropospheric loss of MVK-oxide. Previous modelling work has indicated that CIs are responsible for between 10-70% of all SO_2-initiated oxidation to sulfuric acid (15, 16, 50, 51). Neglecting the reaction of MVK-oxide + SO_2 leads to an 11% decrease in the tropospheric concentration of SO_3 globally, significantly impacting modelled sulfuric acid. For example, over the Amazon region, where isoprene emissions and subsequently MVK-oxide concentrations are highest, the reaction of MVK-oxide + SO_2 contributes up to 20% of sulfuric acid production. This source has modest implications for sulfate aerosol formation (see SI Appendix).

The present work demonstrates that the reaction of the globally dominant and resonance stabilized CI, *syn*-MVK-oxide, with formic acid, is rapid. Evaluation of STOCHEM-CI0 reveals that reaction with MVK-oxide leads to up to 20% reduction in modelled formic acid globally (Figure 8, lower panel). Furthermore, the reactions of organic acids with CIs may contribute to the production of secondary organic aerosols via the formation of low volatility, highly oxygenated products (19).

Conclusions

The direct UV-Vis absorption spectrum of the four-carbon, resonance-stabilized CI, MVK-oxide, has been recorded at 298 K in two independent experiments. We observe broad absorption centered around 370 nm in both experiments, in good agreement with the work of Vansco *et al.* (31), with differences attributed to the different conformer distribution in the 298 K and jet-cooled experiments. The different conformer distribution observed in the 298 K experiments suggest a low yield of stabilized *anti*-MVK-oxide and/or faster *anti*-MVK-oxide decomposition possibly due to internal excitation. The experimentally observed lifetime of MVK-oxide in the 298 K experiments is consistent with *syn*-conformers and substantiates rapid removal of *anti*-conformers as indicated by calculations of Barber *et al.* (6, 30).

Computation and direct experimental kinetic measurements of bimolecular reactions of *syn*-MVK-oxide demonstrate slow *syn*-MVK-oxide removal in the presence of water, confirming recent theoretical predictions (6, 45). Rapid reactivity with SO_2 and formic acid were observed and predicted theoretically, similar to C1-C3 alkyl substituted CIs (10, 11, 18, 19, 37). Complementary MPIMS measurements of the products from SO_2 and formic acid reactions with MVK-oxide indicate the potential role of these reactions in tropospheric particulate formation. SO_3 is observed from the reaction of *syn*-MVK-oxide with SO_2; global chemistry and transport modelling reveal a modest impact on predicted particle nucleation events due to the formation of sulfuric acid. The formation of a highly oxygenated organic hydroperoxide species, resulting from insertion of the CI into the acidic O-H bond, was observed from the reaction of MVK-oxide

with formic acid – recent chamber work has implicated similar species in the formation of secondary organic aerosols (52).

Methods and Materials
UV-Vis absorption spectra and bimolecular rate coefficients for MVK-oxide were recorded using two independent transient absorption experiments, both of which have been described in detail previously. Further details of both the Sandia and IAMS experiments are given in the SI Appendix. Complementary experiments to identify the products of the MVK-oxide + SO_2 and formic acid reactions, and to obtain the kinetics for MVK-oxide formation were undertaken using multiplexed photoionization mass spectrometry, described previously and in the SI Appendix. For all the work reported herein, MVK-oxide was generated using the method of Barber *et al*. (30) using 1,3-diiodobut-2-ene photolysis in the presence of excess O_2. All experiments were performed under pseudo-first-order conditions, such that $[O_2] \gg$ [1,3-diiodobut-2-ene], and for bimolecular kinetics investigations, [co-reactant] $\gg$ [MVK-oxide]. *Ab initio* kinetics calculations were performed to supplement each of the experimental observations. They were based on a combination of density functional theory based rovibrational analyses, coupled cluster-based energy evaluations, variational transition state theory, and master equation analyses that explicitly treat hindered rotational motions. Further details are provided in the SI Appendix. Modelling work was undertaken using STOCHEM-CRI which comprises a global chemistry transport model (STOCHEM) coupled with the common representative intermediate mechanism (CRI). This has been described previously and detailed further in the SI Appendix.

Data Availability Statement.
All data discussed in the paper are available in the main text and SI Appendix.

References

1.   C. Wiedinmyer, X. Tie, A. Guenther, R. Neilson, C. Granier, Future changes in biogenic isoprene emissions: how might they affect regional and global atmospheric chemistry? *Earth Interactions* **10**, 1-19 (2006).
2.   T. B. Nguyen *et al.*, Atmospheric fates of Criegee intermediates in the ozonolysis of isoprene. *Physical Chemistry Chemical Physics* **18**, 10241-10254 (2016).
3.   R. Criegee, Mechanism of ozonolysis. *Angewandte Chemie International Edition in English* **14**, 745-752 (1975).
4.   M. Khan, C. Percival, R. Caravan, C. Taatjes, D. Shallcross, Criegee intermediates and their impacts on the troposphere. *Environmental Science: Processes & Impacts* **20**, 437-453 (2018).
5.   A. Novelli *et al.*, Estimating the atmospheric concentration of Criegee intermediates and their possible interference in a FAGE-LIF instrument. *Atmospheric Chemistry and Physics* **17**, 7807-7826 (2017).
6.   L. Vereecken, A. Novelli, D. Taraborrelli, Unimolecular decay strongly limits the atmospheric impact of Criegee intermediates. *Physical Chemistry Chemical Physics* **19**, 31599-31612 (2017).
7.   M. A. H. Khan *et al.*, An estimation of the levels of stabilized Criegee intermediates in the UK urban and rural atmosphere using the steady-state approximation and the potential effects of these intermediates on tropospheric oxidation cycles. *International Journal of Chemical Kinetics* **49**, 611-621 (2017).
8.   R. Chhantyal-Pun *et al.*, Firect Kinetic and Atmospheric Modeling Studies of Criegee Intermediate Reactions with Acetone. *ACS Earth Space Chem* **3**, 2363-2371 (2019).
9.   C. A. Taatjes *et al.*, Direct observation of the gas-phase Criegee intermediate (CH_2OO). *Journal of the American Chemical Society* **130**, 11883-11885 (2008).
10.   C. A. Taatjes *et al.*, Direct measurements of conformer-dependent reactivity of the Criegee intermediate CH_3CHOO. *Science* **340**, 177-180 (2013).
11.   O. Welz *et al.*, Direct kinetic measurements of Criegee intermediate (CH_2OO) formed by reaction of CH_2I with O_2. *Science* **335**, 204-207 (2012).
12.   F. Liu, J. M. Beames, A. M. Green, M. I. Lester, UV spectroscopic characterization of dimethyl- and ethyl-substituted carbonyl oxides. *J Phys Chem A* **118**, 2298-2306 (2014).
13.   R. Cox, S. Penkett, Aerosol formation from sulphur dioxide in the presence of ozone and olefinic hydrocarbons. *J Chem Soc Faraday Trans* **68**, 1735-1753 (1972).
14.   R. A. Cox, S. A. Penkett, Oxidation of atmospheric SO_2 by products of the ozone–olefin reaction. *Nature* **230**, 321-322 (1971).
15.   M. Boy *et al.*, Oxidation of SO_2 by stabilized Criegee intermediate (sCI) radicals as a crucial source for atmospheric sulphuric acid concentrations. *Atmos. Chem. Phys.* **12**, 27693-27736 (2012).
16.   R. Mauldin *et al.*, A new atmospherically relevant oxidant of sulphur dioxide. *Nature* **488**, 193 (2012).
17.   C. J. Percival *et al.*, Regional and global impacts of Criegee intermediates on atmospheric sulphuric acid concentrations and first steps of aerosol formation. *Faraday Discuss* **165**, 45-73 (2013).
18.   O. Welz *et al.*, Rate coefficients of C1 and C2 Criegee intermediate reactions with formic and acetic acid near the collision limit: direct kinetics measurements and atmospheric implications. *Angew Chem* **53**, 4547-4550 (2014).
19.   R. Chhantyal-Pun *et al.*, Criegee intermediate reactions with carboxylic acids: a potential source of secondary organic aerosol in the atmosphere. *ACS Earth Space Chem* **2**, 833-842 (2018).
20.   C. A. Taatjes *et al.*, Reaction of perfluorooctanoic acid with Criegee intermediates and implications for the atmospheric fate of perfluorocarboxylic acids. *Environ Sci Technol* **53**, 1245-1251 (2019).

21. B. Long, J. L. Bao, D. G. Truhlar, Atmospheric chemistry of Criegee intermediates: unimolecular reactions and reactions with water. *J Am Chem Soc* **138**, 14409-14422 (2016).
22. M. J. Newland *et al.*, Atmospheric isoprene ozonolysis: impacts of stabilised Criegee intermediate reactions with SO_2, H_2O and dimethyl sulfide. *Atmos. Chem. Phys.* **15**, 9521-9536 (2015).
23. L.-C. Lin *et al.*, Competition between H_2O and $(H_2O)_2$ reactions with CH_2OO/CH_3CHOO. *Phys Chem Chem Phys* **18**, 4557-4568 (2016).
24. J. Anglada, J. Gonzalez, M. Torrent-Sucarrat, Effects of the substituents on the reactivity of carbonyl oxides. A theoretical study on the reaction of substituted carbonyl oxides with water. *Phys Chem Chem Phys* **13**, 13034-13045 (2011).
25. J. M. Anglada, P. Aplincourt, J. M. Bofill, D. Cremer, Atmospheric formation of OH radicals and H_2O_2 from alkene ozonolysis under humid conditions. *ChemPhysChem* **3**, 215-221 (2002).
26. A. B. Ryzhkov, P. A. Ariya, A theoretical study of the reactions of parent and substituted Criegee intermediates with water and the water dimer. *Phys Chem Chem Phys* **6**, 5042-5050 (2004).
27. L. Sheps, A. M. Scully, K. Au, UV absorption probing of the conformer-dependent reactivity of a Criegee intermediate CH_3CHOO. *Phys Chem Chem Phys* **16**, 26701-26706 (2014).
28. L.-C. Lin, W. Chao, C.-H. Chang, K. Takahashi, Temperature dependence of the reaction of anti-CH_3CHOO with water vapor. *Phys Chem Chem Phys* **18**, 28189-28197 (2016).
29. D. Zhang, W. Lei, R. Zhang, Mechanism of OH formation from ozonolysis of isoprene: kinetics and product yields. *Chem Phys Lett* **358**, 171-179 (2002).
30. V. P. Barber *et al.*, Four-carbon Criegee intermediate from isoprene ozonolysis: methyl vinyl ketone oxide synthesis, infrared spectrum, and OH production. *J Am Chem Soc* **140**, 10866-10880 (2018).
31. M. F. Vansco, B. Marchetti, M. I. Lester, Electronic spectroscopy of methyl vinyl ketone oxide: a four-carbon unsaturated Criegee intermediate from isoprene ozonolysis. *J Chem Phys* **149**, 244309 (2018).
32. L. Vereecken, H. Harder, A. Novelli, The reaction of Criegee intermediates with NO, RO_2, and SO_2, and their fate in the atmosphere. *Phys Chem Chem Phys* **14**, 14682-14695 (2012).
33. L. Sheps, Absolute ultraviolet absorption spectrum of a Criegee intermediate CH_2OO. *J Phys Chem Lett* **4**, 4201-4205 (2013).
34. L. Sheps, D. W. Chandler (2013) Time-resolved broadband cavity-enhanced absorption spectroscopy for chemical kinetics. (Sandia National Laboratories (SNL-CA), Livermore, CA (United States)).
35. M.-N. Su, J. J.-M. Lin, Note: A transient absorption spectrometer using an ultra bright laser-driven light source. *Rev Sci Instrum* **84**, 086106 (2013).
36. K. T. Kuwata, L. C. Valin, A. D. Converse, Quantum chemical and master equation studies of the methyl vinyl carbonyl Oxides formed in isoprene ozonolysis. *J Phys Chem A* **109**, 10710-10725 (2005).
37. R. Chhantyal-Pun *et al.*, Direct measurements of unimolecular and bimolecular reaction kinetics of the Criegee intermediate $(CH_3)_2COO$. *J Phys Chem A* **121**, 4-15 (2017).
38. D. Stone, M. Blitz, L. Daubney, N. U. Howes, P. Seakins, Kinetics of CH_2OO reactions with SO_2, NO_2, NO, H_2O and CH_3CHO as a function of pressure. *Phys Chem Chem Phys* **16**, 1139-1149 (2014).
39. P. Spietz, J. C. G. Martín, J. P. Burrows, Spectroscopic studies of the I_2/O_3 photochemistry: part 2. Improved spectra of iodine oxides and analysis of the IO absorption spectrum. *J Photochem Photobiol A* **176**, 50-67 (2005).
40. J. Burkholder *et al.* (2015) Chemical kinetics and photochemical data for use in atmospheric studies: evaluation number 18, JPL Publication 15-10. (Jet Propulsion Laboratory, Pasadena).
41. Y. Liu *et al.*, A kinetic study of the CH_2OO Criegee intermediate reaction with SO_2, $(H_2O)_2$, CH_2I_2 and I atoms using OH laser induced fluorescence. *Phys Chem Chem Phys* **19**, 20786-20794 (2017).
42. H.-L. Huang, W. Chao, J. J.-M. Lin, Kinetics of a Criegee intermediate that would survive high humidity and may oxidize atmospheric SO_2. *Proc Natl Acad Sci* **112**, 10857-10862 (2015).
43. L. Vereecken, The reaction of Criegee intermediates with acids and enols. *Phys Chem Chem Phys* **19**, 28630-28640 (2017).
44. R. Chhantyal-Pun *et al.*, Experimental and computational studies of Criegee intermediate reactions with NH_3 and CH_3NH_2. *Phys Chem Chem Phys* **21**, 14042-14052 (2019).

45. J. M. Anglada, A. Solé, Impact of the water dimer on the atmospheric reactivity of carbonyl oxides. *Phys Chem Chem Phys* **18**, 17698-17712 (2016).
46. L. Sheps *et al.*, The reaction of Criegee intermediate CH_2OO with water dimer: primary products and atmospheric impact. *Phys Chem Chem Phys* **19**, 21970-21979 (2017).
47. W. Chao, J.-T. Hsieh, C.-H. Chang, J. J.-M. Lin, Direct kinetic measurement of the reaction of the simplest Criegee intermediate with water vapor. *Science* **347**, 751-754 (2015).
48. Y. Fang, V. P. Barber, S. J. Klippenstein, A. B. McCoy, M. I. Lester, Tunneling effects in the unimolecular decay of $(CH_3)_2COO$ Criegee intermediates to OH radical products. *J Chem Phys* **146**, 134307 (2017).
49. M. C. Smith, W. Chao, K. Takahashi, K. A. Boering, J. J.-M. Lin, Unimolecular decomposition rate of the Criegee intermediate $(CH_3)_2COO$ measured directly with UV absorption spectroscopy. *J Phys Chem A* **120**, 4789-4798 (2016).
50. G. Sarwar *et al.*, Impact of sulfur dioxide oxidation by Stabilized Criegee Intermediate on sulfate. *Atmos Environ* **85**, 204-214 (2014).
51. J. Li, Q. Ying, B. Yi, P. Yang, Role of stabilized Criegee intermediates in the formation of atmospheric sulfate in eastern United States. *Atmos Environ* **79**, 442-447 (2013).
52. Y. Sakamoto, S. Inomata, J. Hirokawa, Oligomerization reaction of the Criegee intermediate leads to secondary organic aerosol formation in ethylene ozonolysis. *J Phys Chem A* **117**, 12912-12921 (2013).
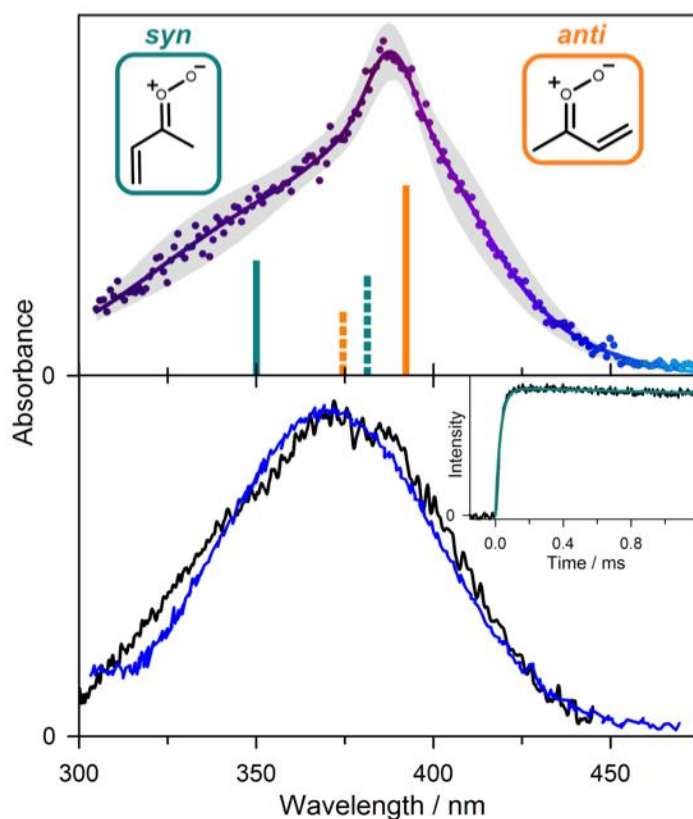
Figures

Figure 1. (Upper panel) Electronic spectrum of MVK-oxide recorded under jet-cooled conditions by the UV-Vis induced depletion method from Vansco *et al.* (31). Data are reproduced from Vansco MF, Marchetti B, & Lester MI (2018) Electronic spectroscopy of methyl vinyl ketone oxide: a four-carbon unsaturated Criegee intermediate from isoprene ozonolysis. *The Journal of Chemical Physics* 149(24):244309, with the permission of AIP Publishing. (Lower panel, main) Direct absorption spectra obtained for MVK-oxide at 298 K using the Sandia broadband multi-pass transient absorption spectrometer (black) and IAMS absorption instrument (blue). Vertical excitation energies and associated oscillator strengths (bars, upper panel) computed for the first $\pi^*\leftarrow\pi$ transition of MVK-oxide are shown for *syn-* (cyan) and *anti-* (orange) conformers; solid and dashed lines further distinguish between *trans* and *cis* configurations, respectively, which rapidly interconvert at 298 K. (Lower panel, inset) Kinetic time trace for MVK-oxide from the Sandia experiment (under 298 K, 10 Torr He; black) integrated between 330-367 nm compared with the simulated thermal unimolecular decay for *syn-*conformers to 2-hydroperoxyl-buta-1,3-diene (cyan) with $k(T)$ = 33 s^{-1} . Thermal rates are computed using *ab initio* master equation modeling in the high-pressure limit (30). The simulations include an experimental rise time for MVK-oxide appearance of 30 μs from the reaction of the iodoalkenyl radical with O_2 (see SI Appendix).
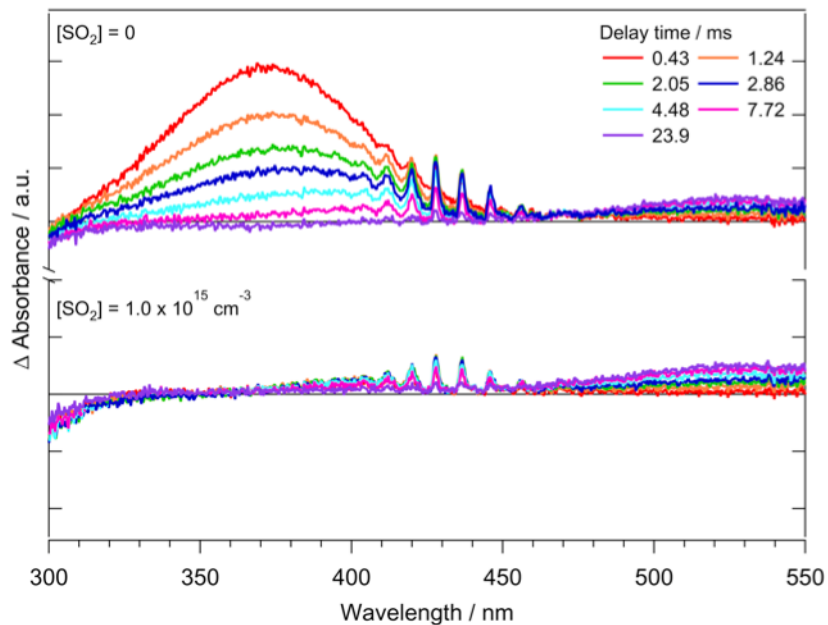
Figure 2. Time-resolved difference absorption spectra recorded at 298 K and 7.4 Torr in the IAMS experiment resulting from (upper panel) the photolysis of 1,3-diiodobut-2-ene in the presence of O_2 and (lower panel) subsequent addition of $[SO_2] = 1.0 \times 10^{15}$ cm^{-3}. In addition to MVK-oxide, the transient spectra contain the spectral signatures of side-products including IO and I_2 (see main text).
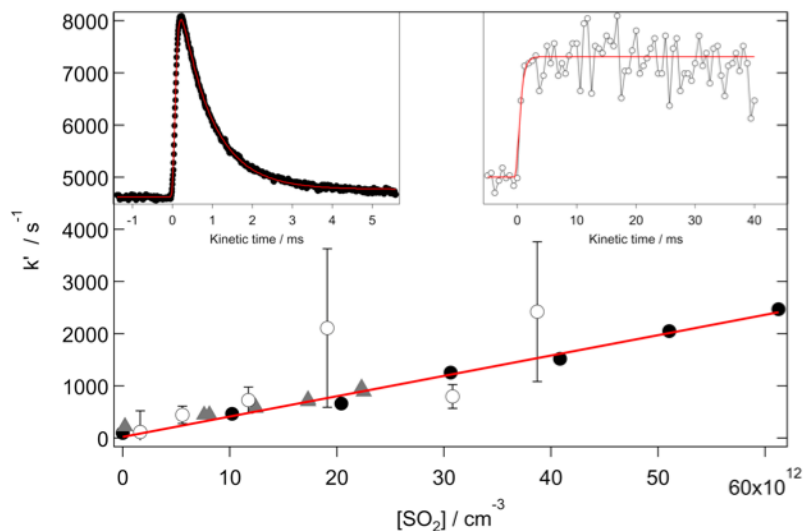
Figure 3. First order rate coefficients for the reaction of *syn*-MVK-oxide with SO_2 as a function of $[SO_2]$, obtained from the decay of *syn*-MVK-oxide using the Sandia absorption experiment (black closed circles, 10 Torr total pressure with He bath gas, 95% confidence limit error bars), the IAMS absorption experiment (grey closed triangles, 4.1 Torr total pressure with O_2 bath gas, 340 nm probe wavelength, 95% confidence limit error bars) and SO_3 growth from the Sandia MPIMS experiment (open black circles, 10 Torr total pressure with He bath gas, 1σ error bars). Note that error bars for the black closed circles and grey closed trianges are smaller than the symbols. The red line is a linear fit to the Sandia absorption data, weighted by the 95% confidence limit error bars, obtaining a bimolecular rate coefficient of $(3.9 \pm 0.5) \times 10^{-11}$ cm^3 s^{-1}. Inset are typical time-resolved traces from the reaction of *syn*-MVK-oxide with SO_2: *syn*-MVK-oxide (Sandia absorption, 330-367 nm, top left) and SO_3 (Sandia MPIMS, 13 eV ionization energy, top right).
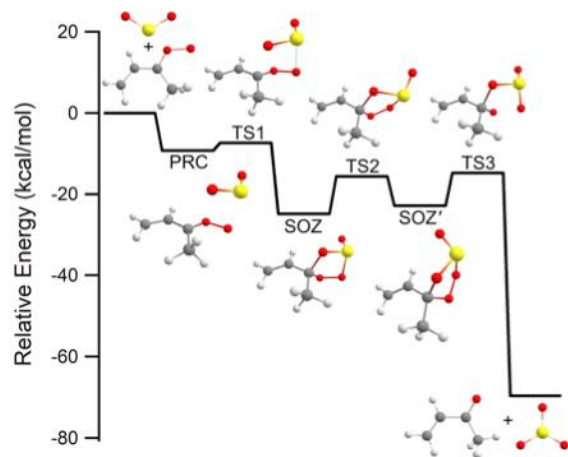
Figure 4. Computed reaction coordinate of the *syn-trans*;*endo* path for the reaction *syn*-MVK-oxide with SO$_2$ at the CCSD(T)/CBS//B2PLYP-D3/cc-pVTZ level with estimated T(A) corrections (see SI Appendix). The reaction proceeds through a pre-reactive complex (PRC) that forms secondary ozonides (SOZ and SOZ') via submerged barriers (TS1 and TS2). The SOZ subsequently decomposes in an exothermic reaction via TS3 to MVK + SO$_3$ products.
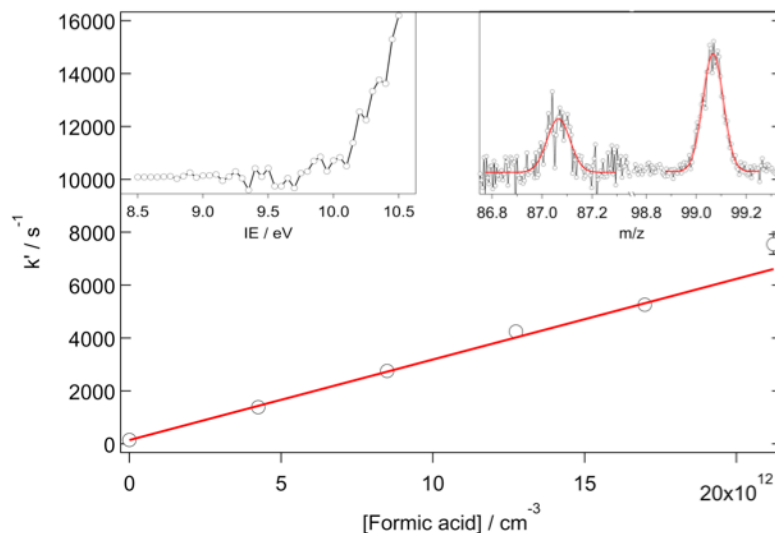
Figure 5. First order rate coefficients for the reaction of *syn*-MVK-oxide with formic acid as a function of formic acid concentration, obtained from the decay of *syn*-MVK-oxide using the Sandia absorption experiment. The red line is a linear fit to the absorption data, weighted by the 95% confidence limit error bars, obtaining a bimolecular rate coefficient of $(3.0 \pm 0.1) \times 10^{-10}$ cm^3 s^{-1}. Note that some of the error bars are smaller than the symbols. Inset (left) is the photoionization spectrum for m/z 99, and (right) the mass spectrum of the proposed daughter ion (DI) products, both obtained using MPIMS. Gaussian fits to the mass peaks yield exact masses of (87.042 ± 0.004) and (99.044 ± 0.001) amu, consistent with the exact masses of 87.045 (MVK-oxide + H, HCO_2-loss DI) and 99.045 (HO_2-loss DI), respectively.
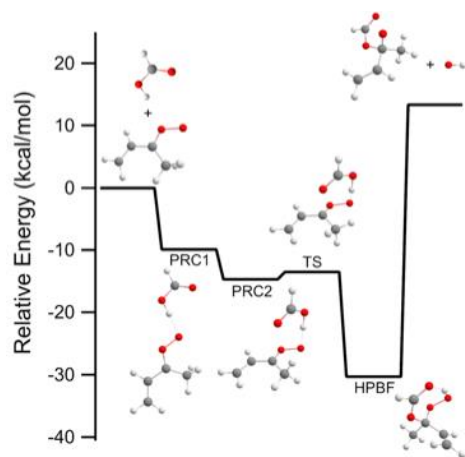
Figure 6. Schematic plot of the reaction pathway for the addition of formic acid to MVK-oxide. Stationary point energies are from CCSD(T)-F12/cc-pVTZ-F12//B2PLYPD3/cc-pVTZ calculations including ZPEs.
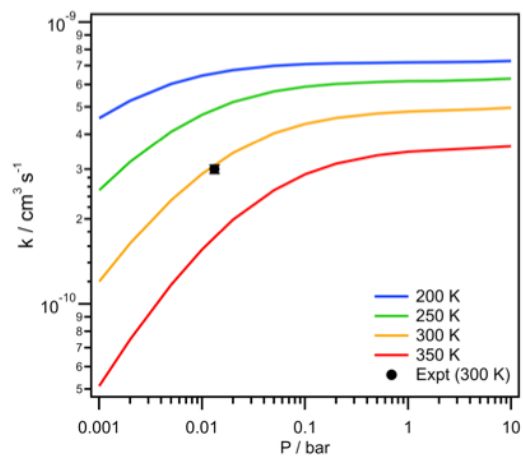
Figure 7. Temperature- and pressure-dependencies of the *syn*-MVK-oxide + formic acid recombination rate coefficient computed based on *ab initio* TST-based master equation modeling. The experimental rate coefficient obtained in this work (solid black circle) is shown for comparison.
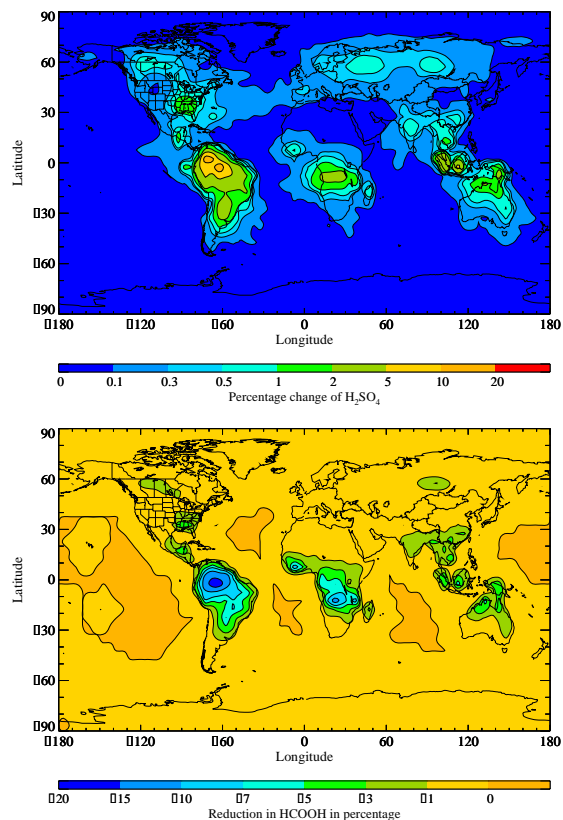
Figure 8. Modelled implications of (upper panel) MVK-oxide reaction with SO$_2$ on global sulfuric acid and (lower panel) MVK-oxide reaction with formic acid on global formic acid evaluated using the global chemistry and transport model STOCHEM-CRI. Model evaluations presented result from comparison of our best current understanding of CI reactions (STOCHEM-CI0) with a case neglecting the contribution of MVK-oxide reactions with SO$_2$ and formic acid, but including unimolecular decomposition, reactions with water and water dimer and unimolecular and bimolecular reactions of all other CIs (STOCHEM-CI1). Further details are given in the SI Appendix.
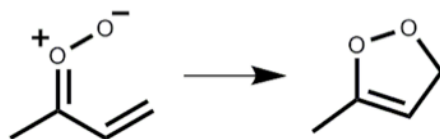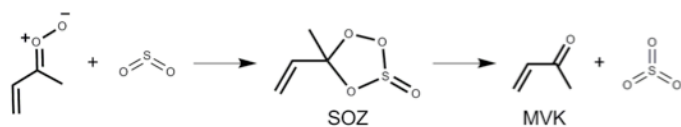
Schemes
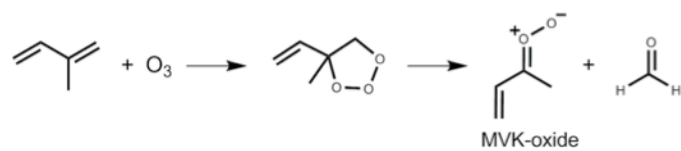
MVK-oxide

Scheme 1. Reaction scheme illustrating the generation of MVK-oxide + formaldehyde from the ozonolysis of isoprene.
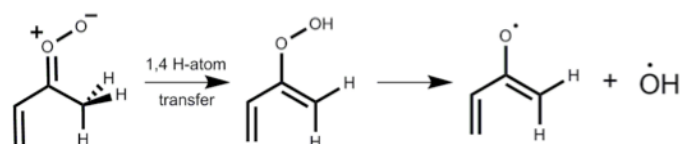
Scheme 2. Reaction mechanism for production of OH from *syn*-MVK oxide *via* 1,4 H-atom transfer to 2-hydroperoxybuta-1,3-diene.

Scheme 3. Unimolecular isomerization of *anti*-MVK-oxide to the cyclic peroxide, dioxole, via 1,5 electrocyclic ring closure.

Scheme 4. Mechanism for the reaction of *syn*-MVK-oxide with SO_2, leading to the formation of methyl vinyl ketone + SO_3 via a secondary ozonide (SOZ).
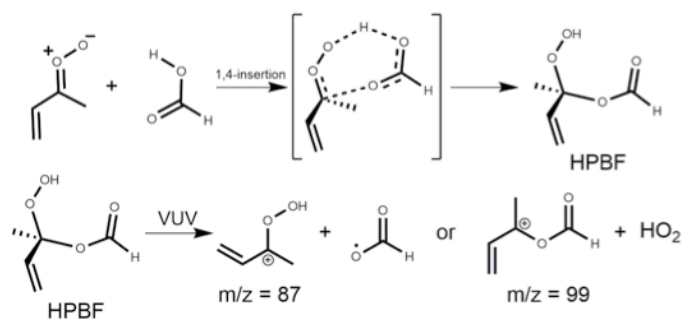
Scheme 5. 1,4-insertion of MVK-oxide into the O-H bond of formic acid, leading to the formation of a functionalized hydroperoxide reaction product.